

A High-Resolution Head and Brain Computer Model for Forward and Inverse EEG Simulation

Alexandra Warner
Advisor: Chris Johnson
University of Utah, Salt Lake City UT

May 15, 2018

1 Introduction

Head models are built and used in many research areas, including imaging, mesh generation, and any bioelectric research topic that requires simulations such as forward and inverse problems.¹ Imaging is necessary for building any head model, and finding a dataset that includes all imaging modalities is rare since most research projects will include only the modalities necessary to their specific project. In each case, a new head model must be built, which is a time consuming task.

In this project, a detailed comprehensive pipeline to build a complete, high-resolution head model is described. Steps include image acquisition, preprocessing and registration, image segmentation, finite element mesh generation, simulations, and visualization. This paper describes two three-dimensional tetrahedral finite element meshes of different resolutions that serve as volume conductors to solve the forward problem. Included are visualizations of the forward problem, with isotropic and anisotropic systems; functional MR data mapped onto a tetrahedral mesh; electroencephalography (EEG) signals mapped onto net electrodes; and diffusion tensor data. Also included is a complete, high-resolution brain segmentation that can be used to create three-dimensional meshes.

Along with outlining the pipeline, this project will be released as an open-source dataset. This project took roughly a year to complete due to the many options in software and techniques, as well as the complexity of the data. Segmentation took roughly 100 hours, most being dedicated to manual editing. Meshing took several weeks to find an appropriate size without holes. Since the segmentation was complex, and high-resolution, the tetrahedral meshes became extremely large, which made for very slow simulations. Further simplification methods failed because of the number of different tissues in the head. Registration of diffusion tensor data and functional MR data was difficult because transformations from other software packages were not compatible with the SCIRun problem solving environment,² and functional MR data has not previously been used in SCIRun.

2 Methods

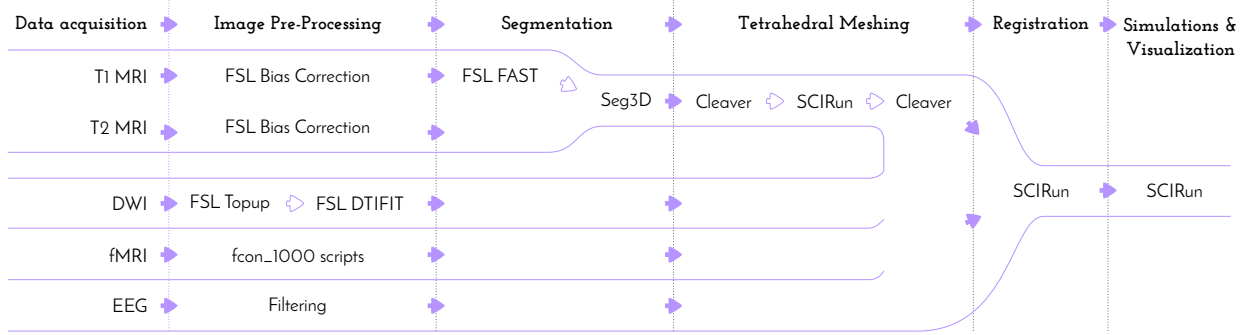


Figure 1: Comprehensive head/brain model pipeline

2.1 Data Acquisition

To construct a high-resolution, personalized, anisotropic volume conductor whole-head model, T_1 -, T_2 - weighted, diffusion weighted, and functional magnetic resonance (MRI) scans were acquired on a healthy, female subject who is 23 years of age on a Skyra 3T full-body scanner (Siemens Medical Solutions, Erlangen, Germany).

The T_1 -weighted scan was performed with a three-dimensional magnetization-prepared, rapid-gradient echo (MPRAGE) sequence.³ The parameters used were as follows: echo time: 3.41ms; repetition time: 2500ms; flip angle: 7 °; resolution matrix size: 256x256 pixels; field of view: 256mm; 208 sagittal slices with a slice thickness of 1mm. Acquisition time was 10:42 minutes.

The T_2 -weighted scan was performed with a sampling prepared with application-optimized contrast using different flip angle evolutions (SPACE) sequence.⁴ The parameters used were as follows: echo time: 406ms; repetition time: 3200ms; resolution matrix size: 256x256 pixels; field of view: 256mm; 208 sagittal slices with a slice thickness of 1mm. Acquisition time was 5:34 minutes. The subject did not move in between the two scans so the scans did not need to be registered.

The diffusion weighted images (DWI) were acquired with multiband two-dimensional echo-planar imaging (EPI).⁵ Both phase encoding directions were performed (anterior to posterior and posterior to anterior) with 64 diffusion directions each. Further sequence parameters for each scan were as follows: echo time: 76.8ms; repetition time: 4070ms; flip angle: 90 °; resolution matrix size: 104x104 pixels; field of view: 208mm; 60 slices with 2.5mm slice thickness. Acquisition time was 5:05 minutes each.

The functional MRI (fMRI) scans were acquired with blood oxygenation level dependent contrast (BOLD). The following parameters were used: echo time: 76.8ms; repetition time: 780ms; flip angle: 55 °; resolution matrix size: 104x104 pixels; field of view: 210mm; 72 slices with 2mm slice thickness. Acquisition time was 10:32 minutes.

A continuous electroencephalogram (EEG) was recorded using a 256-channel HydroCel Geodesic Sensor Net that was connected to a NetAmps 400 amplifier and referenced online to a single vertex electrode shown in Figure 2. Channel impedances were kept at or below 50 kOhms and signals were sampled at 250Hz. The EEG was recorded while the subject sat quietly in a chair, alternating two minute epochs of eyes open and eyes closed for a total of 12 minutes.

All acquisition reports will be included with the dataset.



Figure 2: 256-channel HydroCel Geodesic sensor net on subject

2.2 Preprocessing of Images

2.2.1 MRI Correction

Bias field signal is a low-frequency, smooth signal that corrupts MRI images due to inhomogeneities in the magnetic fields of the MRI machine by blurring images, thereby reducing the high frequencies of the images such as edges and contours. It changes the intensity values of image pixels so that the same tissue has a different distribution of grayscale intensities across the image.⁶ An estimated bias field correction on the T_1 and T_2 MRIs was completed using FMRIB Software Library (FSL) FAST,⁷ which will be described in the Section 2.3. Figure 3 shows FSL's basic user interface, which was used throughout this pipeline.

2.2.2 DWI Distortion Correction

DWIs performed with EPI sequences are prone to distortions from rapid switching of diffusion weighting gradients, movement from the scanning table, and movement from the subject. The diffusion data was collected with reversed phase-encode blips (anterior to posterior (AP) and posterior to anterior(PA)), resulting in pairs of images with distortions going in opposite directions. From these pairs, the susceptibility-induced off-resonance field was estimated using

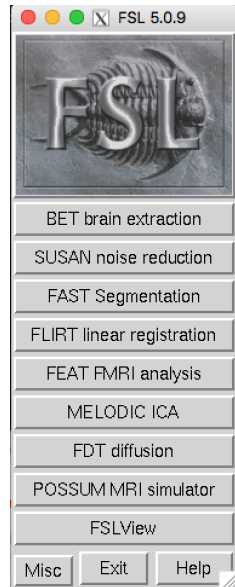


Figure 3: FMRIB software library user interface

a method⁸ similar to what is implemented in FSL.⁹ The two images were combined into a single corrected one using FSL’s topup and eddy command line tools.

Before running these tools, an acquisition parameters text file needed to be created with the FSL-defined total readout time. Two parameters are frequently required to calculate and apply field maps: the effective echo spacing and the total readout time for an EPI sequence. “Effective” echo spacing was used, rather than the actual echo spacing, in order to include the effects of parallel imaging, phase oversampling, etc. It was multiplied by the size of the reconstructed image in the phase direction gave the reciprocal of the effective echo spacing:

$$\text{Effective Echo Spacing (s)} = 1 / (\text{BandwidthPerPixelPhaseEncode} * \text{MatrixSizePhase})$$

The total readout time (FSL definition) is:

$$\text{Total readout time (FSL)} = (\text{MatrixSizePhase} - 1) * \text{EffectiveEchoSpacing}$$

The software package MRIConvert provides the acquisition information about a dicom series, as well as converts to a NiFTI format, including effective echo spacing and total readout time.¹⁰ To obtain this information, the dicom series were loaded for either DWI acquisition were loaded. The selection of “Options?” ensured that the DWI was saved as a NiFTI. Selection of “Convert All” saved all of the files into the output directory specified upon opening MRIConvert. The text file included the FSL-defined total readout time, which was contained in the acquisition parameter file in seconds. MRIConvert also output the b-values and b-vectors files, which were the same for both the DWI AP and DWI PA scans. The last input file required was an “index.txt” file, which contained one column with 65 rows (for 64 directions plus the b0 image) of 1’s.

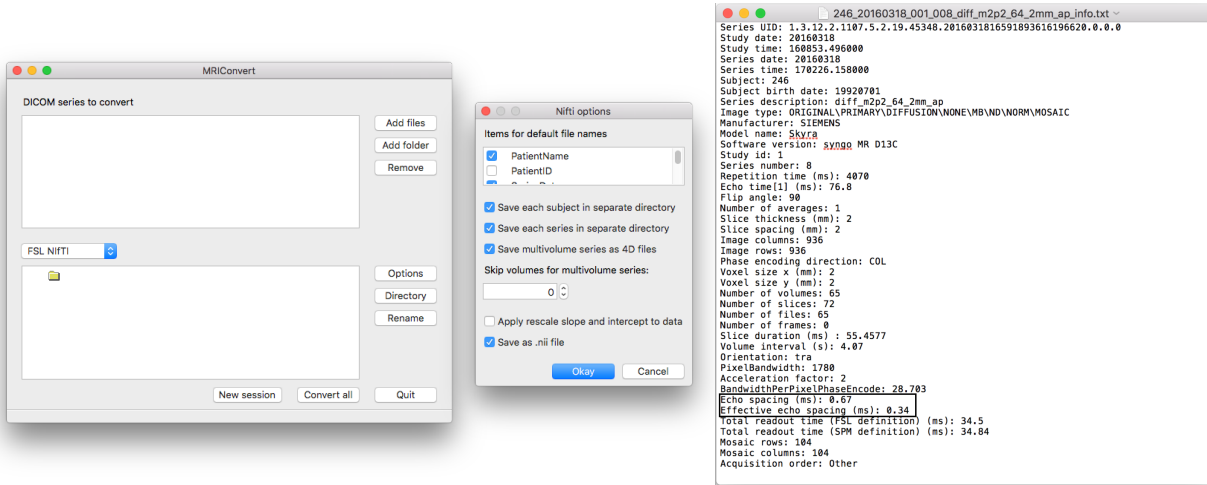


Figure 4: MRIConvert (*left*) with options (*middle*) & output (*right*)

```

0 -1 0 0.0345
0 1 0 0.0345

```

Figure 5: Acquisition parameters text file

A separate folder created for topup results included the following files: the acquisition parameters file; the index file; b-values; b-vectors; and the DWI AP and DWI PA files. In the following instructions, DWI AP was renamed as DWI_up and DWIAP was renamed to DWI_down. The b-values and b-vectors were renamed to dwi.bval and dwi.bvec, respectively. After all files were in place, the following command line commands were executed:

```
fslroi DWI\_up b0\_up 0 1
fslroi DWI\_down b0\_down 0 1

fslmerge -t both\b0\b0\_up\b0\_down

topup --imain=both\b0 --datain=acq_params.txt --config=mine.cnf --out=topup\_results
applytopup --imain=b0\_up,b0\_down --inindex=1,2 --datain=acq_params.txt
--topup=topup\_results --out=b0\_hifi

bet b0\_hifi b0\_hifi\_brain -m -f 0.2
eddy --imain=DWI\_up --mask=b0\_hifi\_brain\_mask --index=index.txt --acqp=acq_params.txt
--bvecs=dwi.bvec --bvals=dwi.bval --fwhm=0 --topup=topup\_results --flm=quadratic
--out=eddy\_unwarped
```

These commands first obtained the b0 image, which is the baseline image used for calculating field maps, for both encoding directions. Then the two b0's were merged together into one file, topup and eddy were applied for distortion correction, and ‘bet’ is applied for brain extraction. The distortion corrected file was named “eddy_unwarped.nii.”

2.2.3 Diffusion Tensor Images

After the DWI images were corrected, diffusion tensor images (DTI) were calculated using FSL’s DTIFIT.¹¹ Upon opening FSL, “FDT Diffusion” was chosen, followed by “DTIFIT Reconstruct diffusion tensors” in the drop down menu and input files manually; Table 1 lists the files selected.

Table 1: DTIFIT input files

Diffusion weighted data	eddy_unwarmed.nii
BET binary brain mask	b0_hifi_brain_mask.nii
Output basename	desired output location
Gradient directions	dwi.bvec
b values	dwi.bval

DTIFIT output the eigenvalues (named L1, L2, and L3) and the eigenvectors (named V1, V2, and V3) for the diffusion tensor field. ITK-SNAP¹² converted the files from NiFTI format to nrrd, although there was a loss of precision. The files were then input into SCIRun to build the tensor field using the eigenvalue and eigenvectors with the network shown in Figure 27. The SCIRun “CalculateFieldData” module requires only two eigenvectors as input because it calculates the third eigenvector automatically since it should be orthogonal to the first two.

The tensor field was built in SCIRun rather than in 3D Slicer¹³ or FSL DTIFIT because the output data would be “backwards” and could not be registered with the mesh in SCIRun.

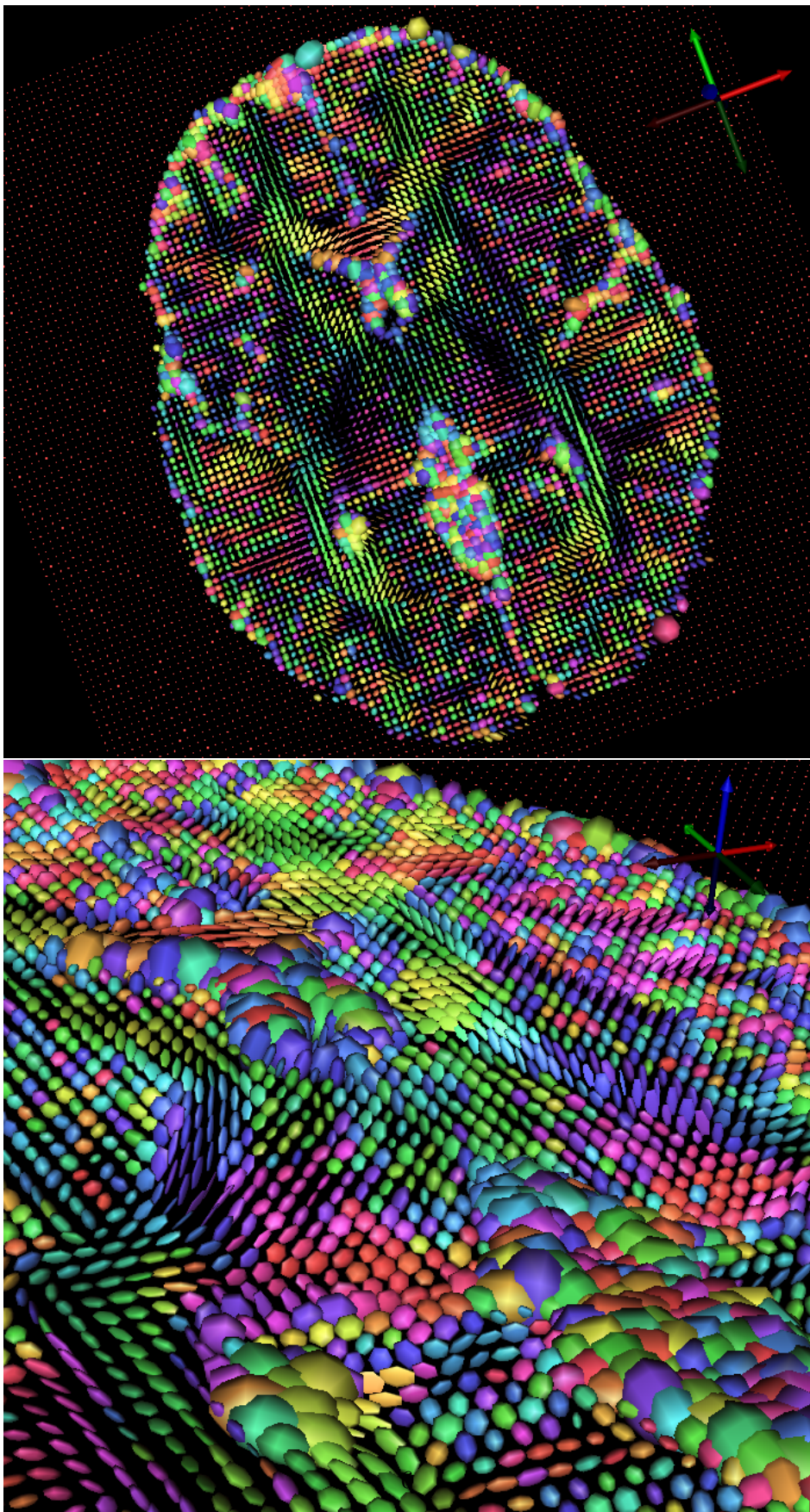


Figure 6: Diffusion tensor visualization using SCIRun

2.2.4 fMRI

fMRI data was preprocessed using the 1000 Functional Connectomes Project pipeline scripts,¹⁴ which perform anatomical preprocessing, functional preprocessing, registration to the T_1 MRI, segmentation, and nuisance signal regress. The outline pipeline used on this fMRI dataset, specific to the University of Utah, can be found at https://bitbucket.org/UtahBrainNetworks/base_prep, and includes instructions for installation, compilation, and usage.

After running fMRI data through the pipeline “rest.nii”, the preprocessed fMRI file, was opened in Matlab using the “load.nii(‘rest.nii’)” function within the NiFTI toolbox.¹⁵ The four-dimensional “img” variable was then resized to a two-dimensional variable and saved to use in SCIRun.

2.2.5 EEG

The filetype of the EEG recordings was in an .edf file after a 60Hz notch filter and its harmonics.¹⁶ The EEG signal matrix was obtained using a Matlab script called “edfRead.m”.¹⁷ To run this script, the following command was used: “[hdr, record] = edfread(fname).” The variable ‘record’ contained the signals. The last two rows of the matrix were removed because they did not correspond to EEG electrodes, as well as the beginning and end of the experiment when the EEG net was being put on and taken off.

2.2.6 Registration

Since the subject did not move in between the T_1 and T_2 MRI, no registration was necessary before segmentation and meshing. The tetrahedral mesh was generated in its own coordinate space from the segmentation, and was registered to the DTI coordinate space with a rigid registration using SCIRun. The fMRI data was registered to the mesh coordinate space with a rigid registration using SCIRun. The fMRI data can use the same transformation matrix used to register the mesh to register to DTI coordinate space later, if desired. The SCIRun networks for registration are included in Section 2.6.

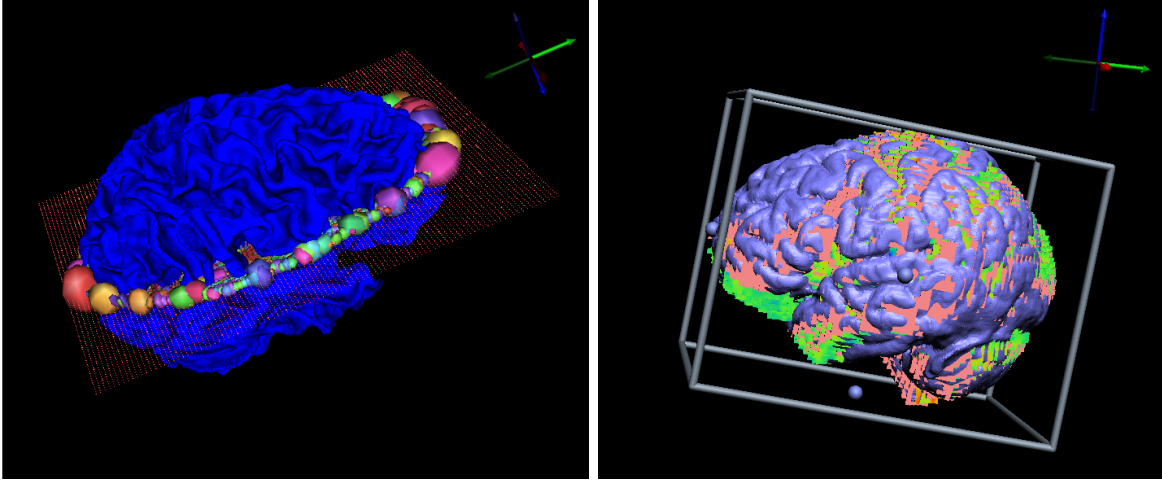


Figure 7: SCIRun manual registrations: mesh to DTI registration (*left*), fMRI to mesh registration (*right*)

2.3 MRI Segmentation of Tissues

Segmentation of the head tissues proved to be the most time-consuming section of the pipeline. The head volume was segmented into air, cerebral spinal fluid (CSF), white matter, grey matter, skull, sinus, eyes, and scalp. Segmentation of the brain can be difficult due to the similar intensities of the different tissues, which means that merely applying a median filter and thresholding the image is not enough. The majority of the segmentation work was done using Seg3D, a free volume segmentation and processing tool.¹⁸

The brain was initially segmented by inputting a skull stripped T_1 MRI into FSL FAST Segmentation. The T_1 MRI was skull stripped using FSL’s brain extraction tool (BET).¹⁹ FAST outputs CSF, white matter, and grey matter layers as well as a bias-corrected T_1 MRI. This method, compared with Freesurfer,²⁰ Statistical Parametric Mapping through Matlab (SPM),²¹ Atlas Based Classification through 3D Slicer,²² and Seg3D methods alone, produced the best initial brain segmentation results for this data.

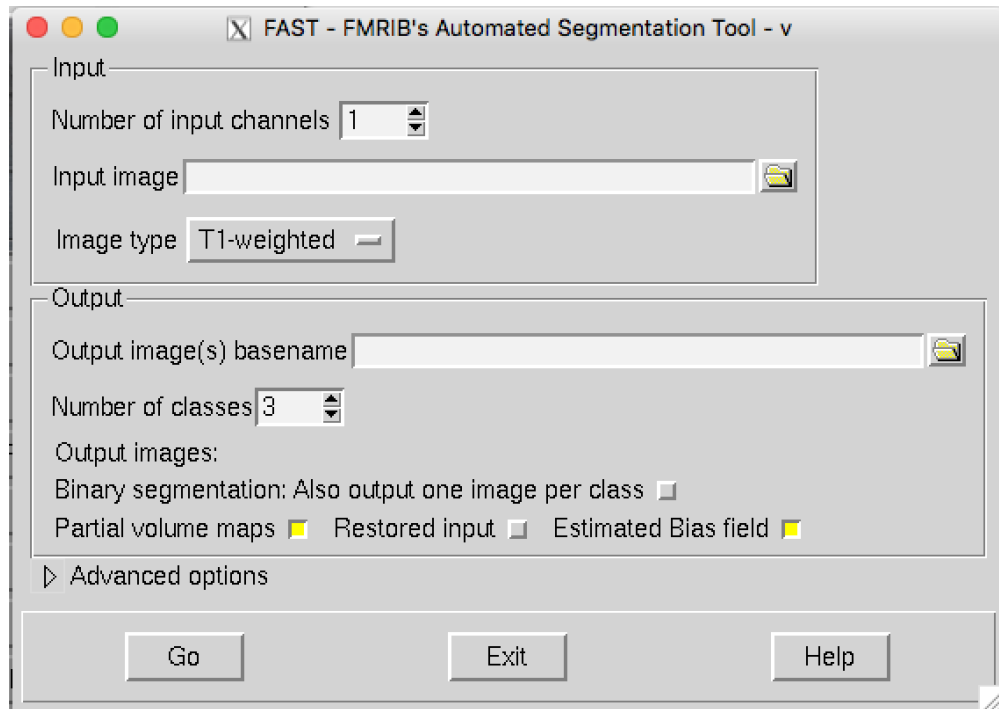


Figure 8: FSL FAST user interface

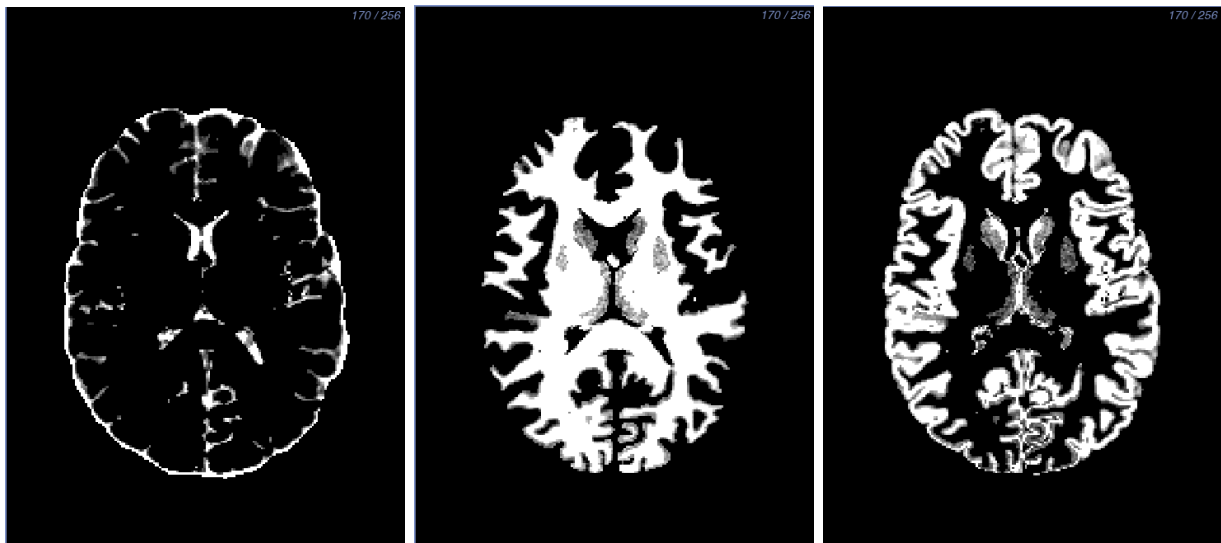


Figure 9: FSL FAST output: CSF (*left*), white matter (*center*), grey matter (*right*)

Although the FSL FAST results were a great improvement compared to the other segmentation software trials, manual segmentation still needed to be done on those layers to add more detail and take out any crossover between the layers. White matter was the first layer to be segmented since it is the innermost layer. First, a threshold layer was created from the FSL FAST output. Every

slice in every direction was inspected and manually edited, adding more detail that could be seen with the naked eye or cleaning up noise from FSL FAST.

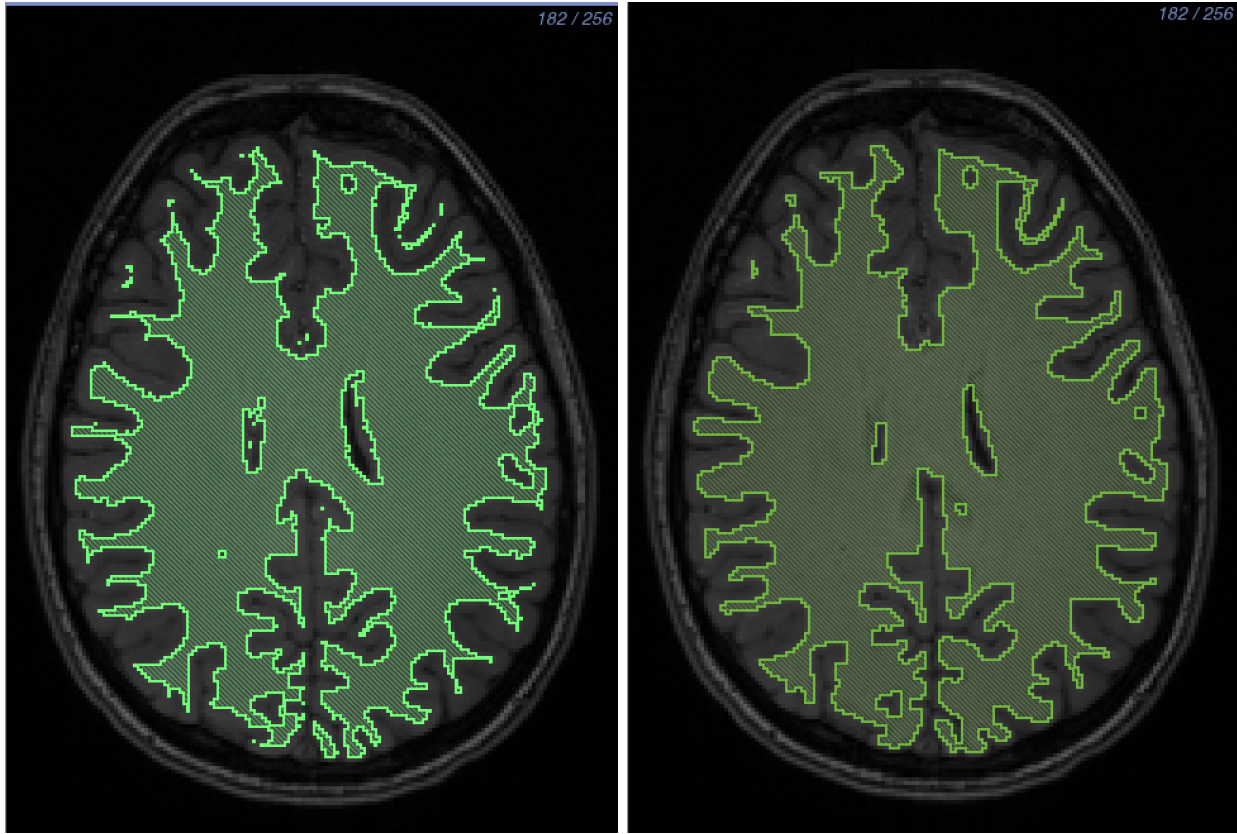


Figure 10: White matter segmentation: Before (*left*) and after (*right*) manual segmentation. The hook feature in the upper, right-hand corner is the most notable change between the two layers. The layer is more full and has less noise.

After the white matter was segmented, a threshold layer for the grey matter was created from the FSL FAST output. Each slice in every direction of the grey matter was also inspected. The white matter layer was removed from the grey matter using a Boolean remove mask filter. Any holes between the two layers were filled manually. More detail was added to the grey matter folds to add to the CSF layer as well. The last part of editing the grey matter was to add a grey matter nuclei to the layer. The thresholding algorithms generated noise around these nuclei, so they were segmented by hand, using the paintbrush tool, and added to the grey matter layer with a Boolean or mask filter. Any overlap of the nuclei in the white matter was removed using a Boolean remove mask filter.

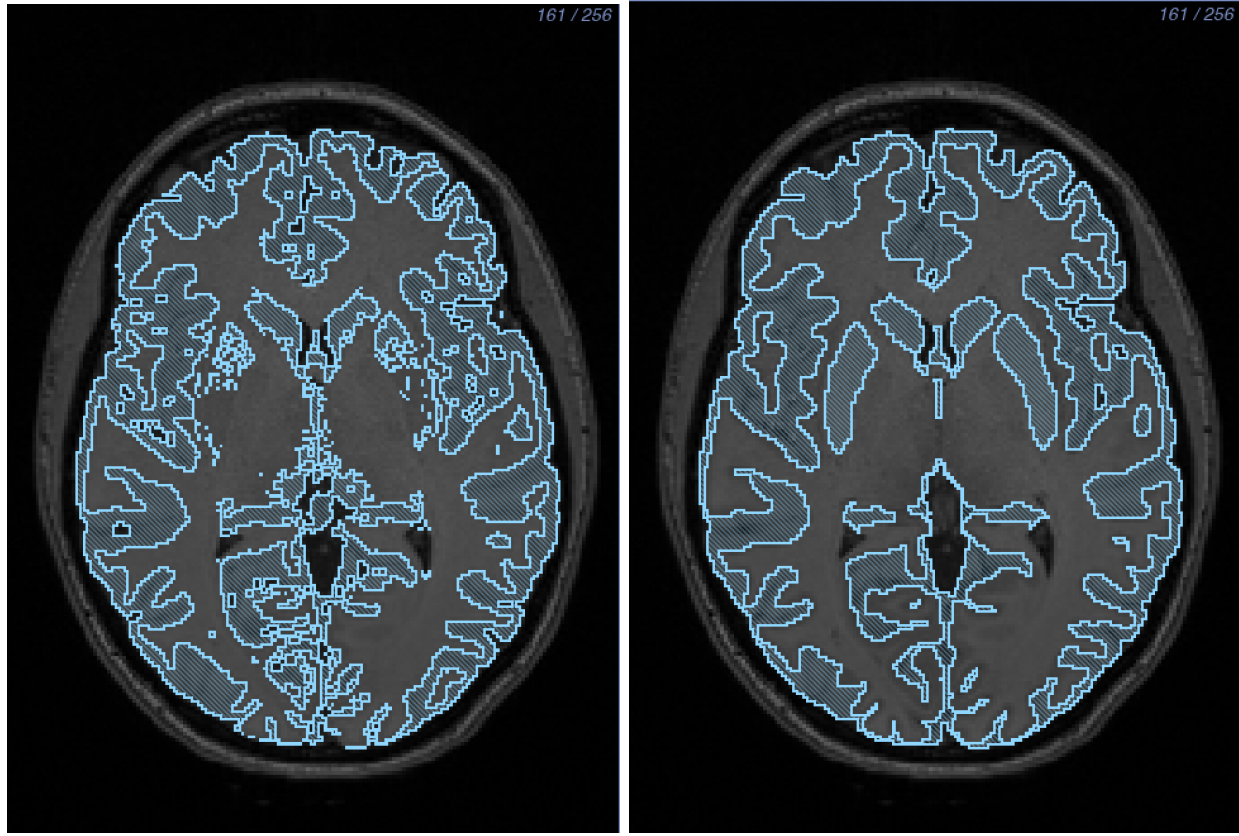


Figure 11: Grey matter segmentation: Before (*left*) and after (*right*) manual segmentation. Grey matter nuclei located in the center of the brain were segmented manually.

After segmentation of the grey and white matter layers was completed, the CSF layer was made by creating a solid threshold layer for the entire brain and removing the white and grey matter layers using a Boolean remove mask filter. The white matter, grey matter, and CSF layers were then checked for holes, whether on the surface or the inside the segmentation. A quality check on the layers was also performed to ensure that the layers were at least two pixels wide. This is an important step for creating a holeless tetrahedral mesh.

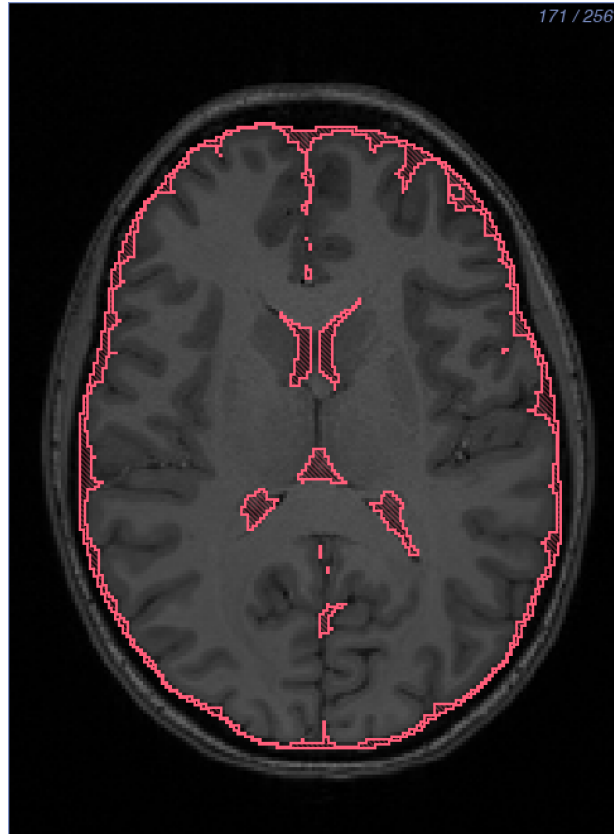


Figure 12: CSF segmentation

The skull and the sinus layers were the most difficult to segment using only an MRI because they both appear black in the image, and the subject did not have a computed tomography (CT) scan. The first attempt to create a bone layer applied FSL's skull stripping function by using the BET2 tool to create a skull. The T_1 MRI was then thresholded to create the remainder of the bones in Seg3D, and then connected to the skull made from FSL. Although this approach gave a decent skull segmentation considering only having an MR image, the method to segment the sinus layer was yet to be determined. As a second method, the skull was estimated from an MR-based synthetic pseudo-CT. An improved iterative version of the patch-based method was used as described by Torrado-Carvajal et al. that takes the T_1 and T_2 images as input, and synthesizes the pseudo-CT based on both images, providing more refined and accurate bone boundaries.²³

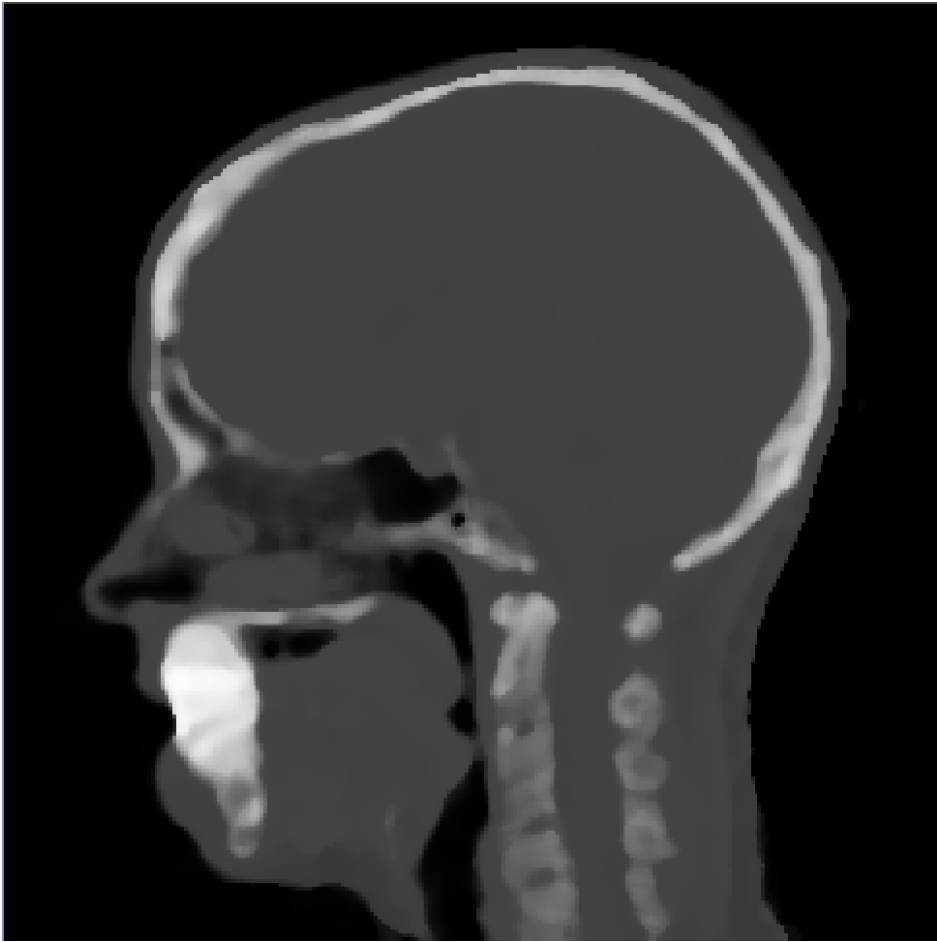


Figure 13: Pseudo-CT scan

The pseudo-CT method gave a good starting place for skull segmentation, but still needed manual editing. After using a median filter with one pixel radius and thresholding, each slice in each direction was manually edited. Since the subject had a permanent retainer in her mouth, the mouth was segmented as solid bone, this was not a concern because the EEG cap used did not cover the subject's mouth. The pseudo-CT image also provided a segmentation of the sinuses and esophagus by thresholding the black pixels. After the thresholding, the sinus layer was also manually edited. Quality checks were done on both layers to ensure that there were no holes and that the layers were at least two pixels thick.

The eyes, skin, and air layers were less time consuming, in comparison, to segment. The eyes were easily segmented by thresholding the T_2 MRI. The skin layer was segmented by thresholding the entire volume and removing all previous layers using a Boolean remove mask filter. A quality check was performed on the skin layer to ensure that it was at least two pixels thick. The important places to check for this are at the bridge of the nose, the bottom of the chin, and the sides of the head. Last, the air was segmented by thresholding the entire image and removing the solid skin layer, followed by a check to ensure that the segmentation did not contain any holes between layers

after they were removed. This final step is imperative to assure a quality mesh.

Table 2: Segmentation Time

Segmented Tissue	Amount of Work (hrs)
White Matter	40
Grey Matter	20
CSF	4
Skull and Sinus	35
Eyes, Scalp, & Air	8

2.4 Finite Element Mesh Generation

Segmentations were used to generate realistic three-dimensional geometries for use in subsequent finite element simulations. A smooth, linear, subject-specific, boundary-conforming, tetrahedral finite element mesh was generated using Cleaver software²⁴ on a Late 2013 Mac Pro with a 2.7 Ghz 12 Core Intel Xeon E5 processor, 64 GB of RAM, and an AMD FirePro graphics card. Cleaver is a multimaterial meshing package that produces structured meshes of tetrahedral elements with guaranteed minimum element angles, resulting in quality meshes that require fewer computational resources. To make a very high-resolution mesh without holes, the parameters listed in Table 3.

Table 3: Clever Settings (High Resolution)

scaling factor	0.6
size multiplier	1.0
lipschitz	0.2
padding	0
element sizing method	adaptive

Along with these parameters, indicator functions had to be input into Cleaver. Indicator functions are created by calculating distance maps of each layer in Seg3D; ensure the distance map is inverted . To reduce the size of the mesh, a new mesh was made with a scaling factor of 1.0 with the remainder of the parameters as described before. The computing sizing field was exported from Cleaver and manipulated in SCIRun by changing how quickly the elements increased in size. The changed sizing field was then input into Cleaver with the same indicator functions and cleaved a new mesh using Cleaver.

2.5 Mathematical Modeling

The head mesh, with associated inhomogeneous and anisotropic regions, was used as a volume conductor to solve the following boundary value problem:

$$\nabla \cdot \sigma \nabla \Phi = -I_V \quad \text{in } \Omega, \quad (1)$$

where Φ is the electrostatic potential, σ is the electrical conductivity tensor, and I_V is the current per unit volume defined within the solution domain, Ω . Equation (1) is solved for Φ with a known

description of I_V and the Neumann boundary condition:

$$\sigma \nabla \Phi \cdot \mathbf{n} = 0 \quad \text{on } \Gamma_T, \quad (2)$$

which says that the normal component of the electric field is zero on the surface interfacing with air (here denoted by Γ_T). The brain and surrounding tissue and skull were discretized, using dipoles for the current source. The electrical field was calculated within the brain and then projected onto the surface of the scalp.²⁵

2.5.1 Electrical Conductivity Preparation

All electrical conductivities were homogeneous for each tissue with the exception of white matter when using tensor data. The isotropic conductivities²⁶ are shown in Table 4.

Table 4: Isotropic Tissue Conductivity

Tissue Type	Isotropic Conductivity (S/m)
White Matter	0.1429
Grey Matter	0.3333
Cerebrospinal Fluid (CSF)	1.79
Skull	0.001
Skin	0.4346
Sinus	1e-6
Eyes	0.5051

When DTI tensor data is added, there are two approaches to converting the tensor data to conductivities. The first is scaling the data:²⁷

$$\sigma_{aniso} = \frac{\sigma_{iso}}{\sqrt[3]{d_1 d_2 d_3}} D \quad (3)$$

where D is the diffusion data, d_i is the i th eigenvalue of D , and σ_{iso} is the white matter isotropic conductivity. The second method gives the white matter a fixed ratio of conductivity:

$$\sigma_{aniso} = \begin{bmatrix} v_1 \\ v_2 \\ v_3 \\ W \end{bmatrix}, W = \begin{bmatrix} \sigma_{iso} \\ \frac{\sigma_{iso}}{10} \\ \frac{\sigma_{iso}}{10} \\ W \end{bmatrix} \quad (4)$$

where v_i is the i th eigenvector of D , W is the white matter ratio vector, and the ratio is 10 : 1.

2.5.2 Numerical Methods

Solutions to Equation 1 were computed using finite element methods. By applying Green's divergence theorem to Equation 1, the following weak formulation was generated:

$$\int ((\bar{\sigma}_e + \bar{\sigma}_i) \nabla \phi_e) \cdot \nabla \psi(\bar{x}) d\bar{x} = - \int (\bar{\sigma}_i \nabla V_m) \cdot \nabla \psi(\bar{x}) d\bar{x}, \quad \forall \psi \in \Omega \quad (5)$$

where Ω is the linear, finite element mesh and ψ represents the finite element basis functions characterized by local hat functions associated with mesh nodes. By applying this formulation to the finite dimensional mesh, we can reduce Equation 5 to a system of linear equations:

$$A\phi_e = -RV_m \quad (6)$$

where A and R represent stiffness matrices defined by $A_{j,k} = \langle \nabla\psi_j, (\bar{\sigma}_e + \bar{\sigma}_i)\nabla\psi_k \rangle_\Omega$ and $R_{j,k} = \langle \nabla\psi_j, \bar{\sigma}_i\nabla\psi_k \rangle_\Omega$, while ϕ_e and V_m represent extracellular and transmembrane potentials, respectively.²⁸

SCIRun, the open-source problem-solving environment, was used to apply parameters and to solve Equation 6 numerically. Within the SCIRun environment, isotropic and anisotropic conductivity tensors were applied to the mesh as well as to inhomogeneous regions. Initial and boundary conditions were defined, and border regions were generated in order to compute potentials by way of a conjugate gradient method with a Jacobi preconditioner.

2.6 Simulations & Visualization

All simulations and visualization were done in the SCIRun problem-solving environment. All networks are shown in Figures 28 - 31.

2.6.1 Forward Problem

Solving systems from a known source to the EEG electrodes, described in Section 2.5, is known as a forward problem. The opposite action, solving systems from the EEG data to a known source, is an inverse problem. Inverse problems are commonly used for subjects with neurological disorders. In this project, SCIRun networks were built to solve forward problems with known sources and to write a lead field matrix for inverse problem networks in the future. The forward problems were solved with an isotropic system and an anisotropic system, which included DTI data.

The necessary inputs for the isotropic case were the tetrahedral head mesh, isotropic conductivities, the head segmentation, the physical electrode locations, and dipole sources. The physical electrode locations and dipole sources were part of the EEG dataset. The fiducials were removed from the electrodes, and the only dipole sources were those chosen by the user. The dataset contained 4800 dipoles, and 256 electrodes after the fiducials are removed. The head mesh was registered to the head segmentation with a rigid registration. After the flat tetrahedra were cut out of the mesh, the conductivities were mapped to their respective tissues. The electrodes and dipoles were registered to the head mesh with the same transform. The system was solved with the mapped data and the chosen dipole sources. The solution was then mapped onto the mesh and the electrodes for visualization. Streamlines and isolines were also included in the visualization.

For the anisotropic case, the network was largely the same with the exception of the diffusion tensor dataset used as white matter conductivities after it was scaled as explained in Section 2.5.1. In addition, the DTI to mesh transform was needed as input. The head mesh, electrodes, and dipoles were registered to the DTI space with a rigid registration; the head segmentation was not needed.

2.6.2 fMRI

The fMRI data was visualized one step at a time using the two-dimensional matrix described in Section 2.2.4 as input and viewing one column at a time. Each column was set onto a lattice volume, which was then rotated 180 degrees, smoothed, thresholded, and clipped for easier rigid registration. The fMRI was registered to the tetrahedral mesh using the bounding boxes and manual registration. After registration, the smoothed fMRI data was mapped onto the mesh using a mapping matrix with a linear interpolation basis.

2.6.3 EEG

The EEG data was visualized on the physical electrode locations, which were registered to the mesh space with a rigid registration after the fiducials were removed from the electrode dataset. The filtered and cut EEG matrix was used as input and each time step was represented as a column. The electrodes were then placed onto the mesh, and the EEG data mapped onto the electrodes one time step at a time.

3 Results

All SCIRun networks used to generate results will be included in an open-source dataset for future use and editing.

3.1 Segmentation

For this project, we segmented an entire head into eight detailed layers which are listed in Section 2.3. We used this mesh to create an inhomogeneous three-dimensional tetrahedral mesh.

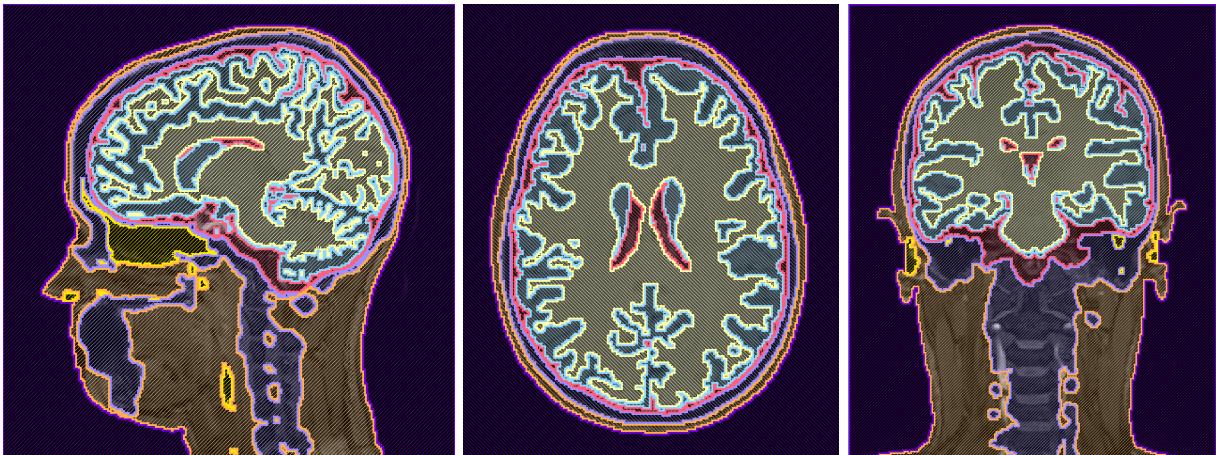


Figure 14: A high-resolution, eight-layer full head segmentation made with Seg3D

As the dataset didn't include a CT scan, the task of segmenting the skull and the sinus layers seemed daunting. As described in Section 2.3, our first attempt at a bone segmentation was to

combine a skull made from FSL²⁹ with bones thresholded using Seg3D. Although we had a bone segmentation, the sinus segmentation would have to be created manually.

The skull/bone and sinus segmentations we made from the pseudo-CT scan were smooth and connected segmentations and fit well into the entire head segmentation. However the teeth and mouth are solid bone due to the subject’s permanent retainer, but this is not concerning as the EEG electrodes didn’t include subject’s mouth.

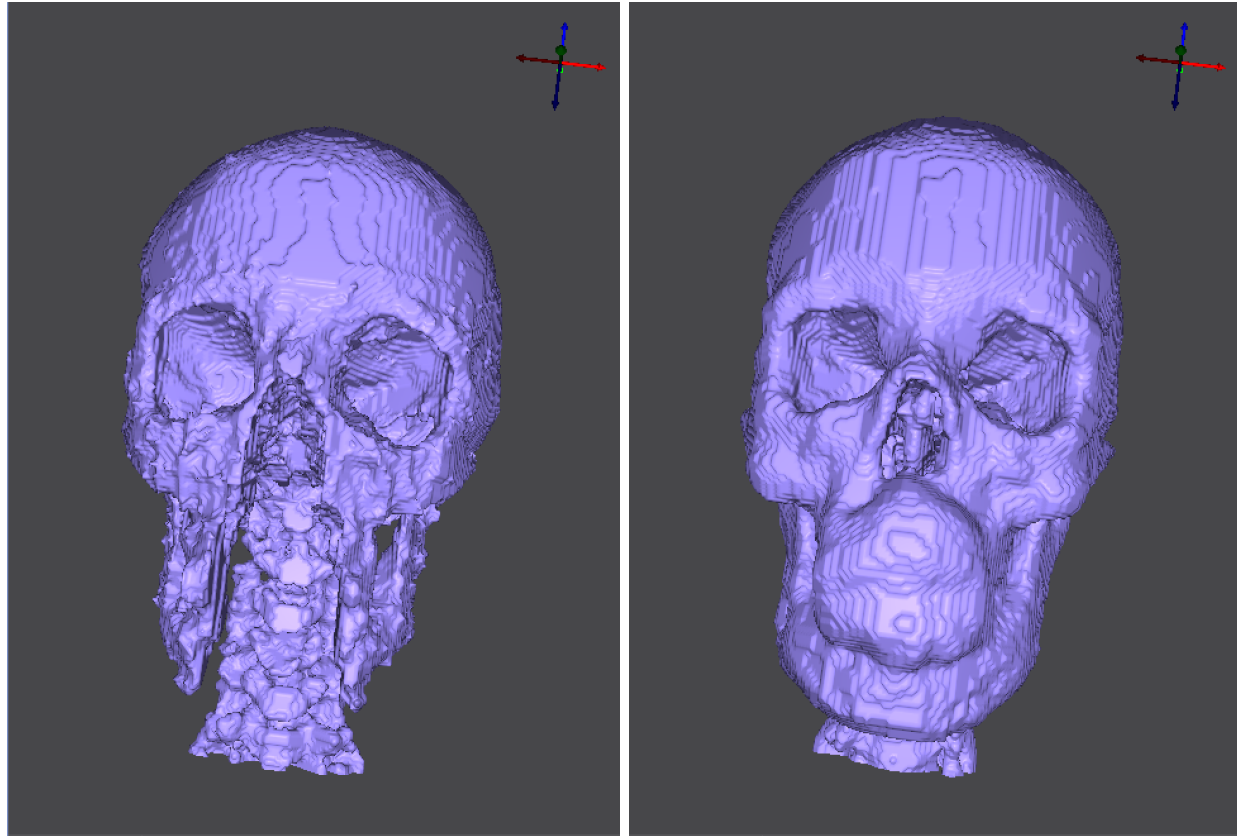


Figure 15: Skull segmentation comparison: Created with BET (*left*) and thresholding and created with pseudo-CT (*right*). Both segmentations were made using Seg3D.

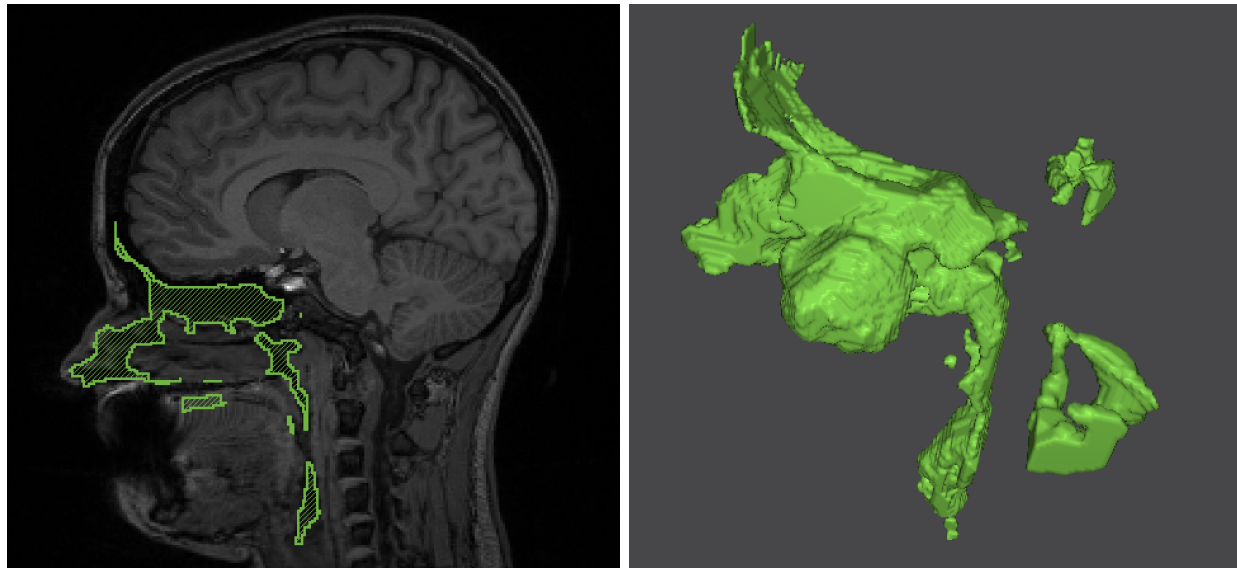


Figure 16: Sinus segmentation

During MRI imaging, the subject was on her back and this caused the brain to shift to the back of the head which resulted in thin segmented sections on the back of the head. There were also thin sections on the side of the subject's head, the bridge of the nose, and the bottom of the chin. We made these sections at least two pixels thick to ensure a mesh without holes.



Figure 17: Thin segmentation sections: side of the head (*left*), bridge of the nose (*middle*), bottom of the chin (*right*)

3.2 Finite Element Meshes

The highest resolution mesh we generated with the settings listed in Section 2.4 had 60.2 million elements and 10.3 million nodes. This mesh was so large due to the complexity of the segmentation including small features, thin sections, and several layers touching at once. The simulations performed slowly when using this mesh due to its size, and required at least 32GB of RAM.

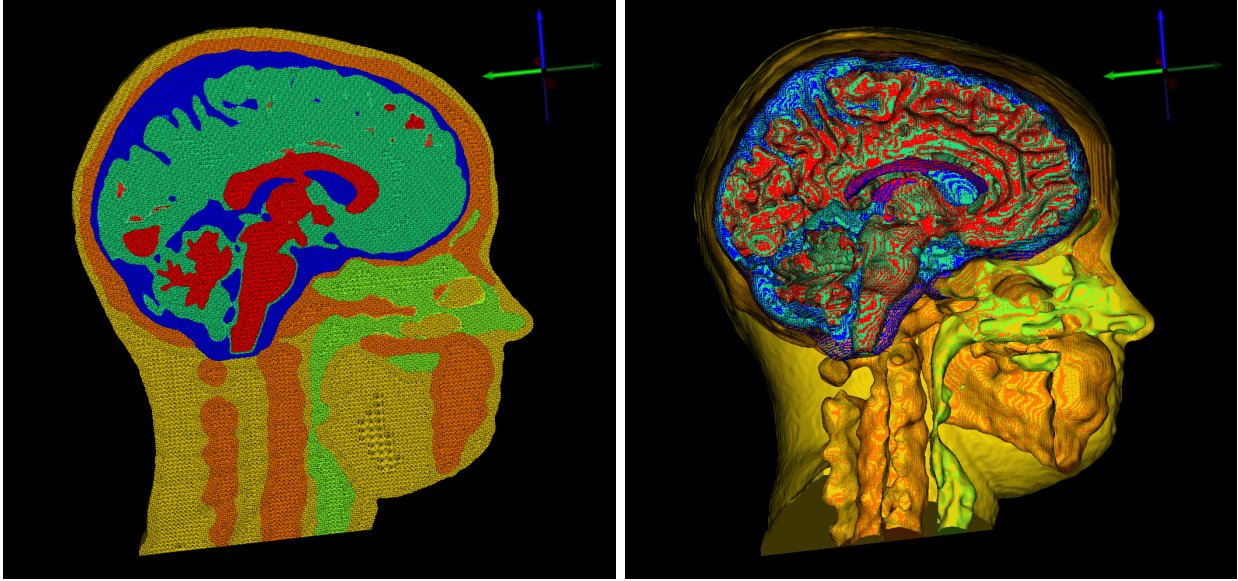


Figure 18: 60.2 M element mesh: tetrahedral mesh (*left*), surface mesh (*right*)

We attempted to generate smaller sized meshes to be able to run simulations more efficiently, but many of the meshes contained holes. After we manually changed the sizing field described in Section 2.4, we generated a mesh with 15.7 million elements and 2.7 million nodes that contained no holes. However this mesh contained one flat tetrahedra, which we later removed in a SCIRun network, and is currently being investigated by Cleaver software developers.

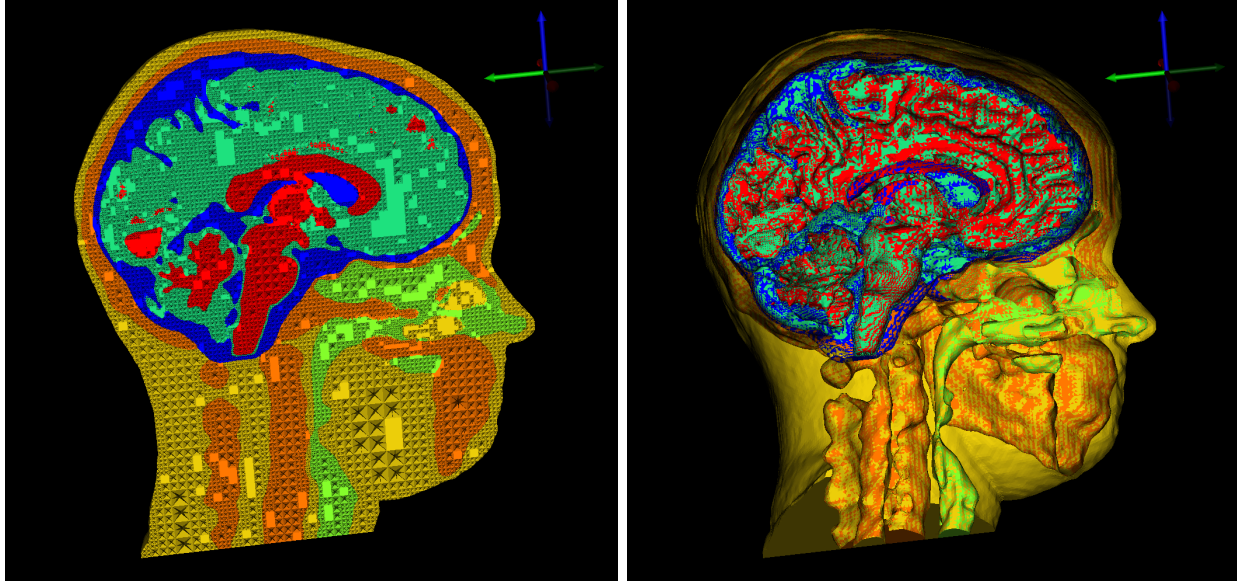


Figure 19: 15.7 M element mesh: tetrahedral mesh (*left*), surface mesh (*right*)

3.3 Forward Problem

3.3.1 Isotropic

An isotropic, inhomogeneous head model is expected to have fairly spherical propagation of electrical signal. We generated three-dimensional streamlines as well as isolines to visualize this propagation and to compare between isotropic and anisotropic conductivity. The simulations showed spherical propagation and acceptable registration of electrodes and dipoles to the mesh space.

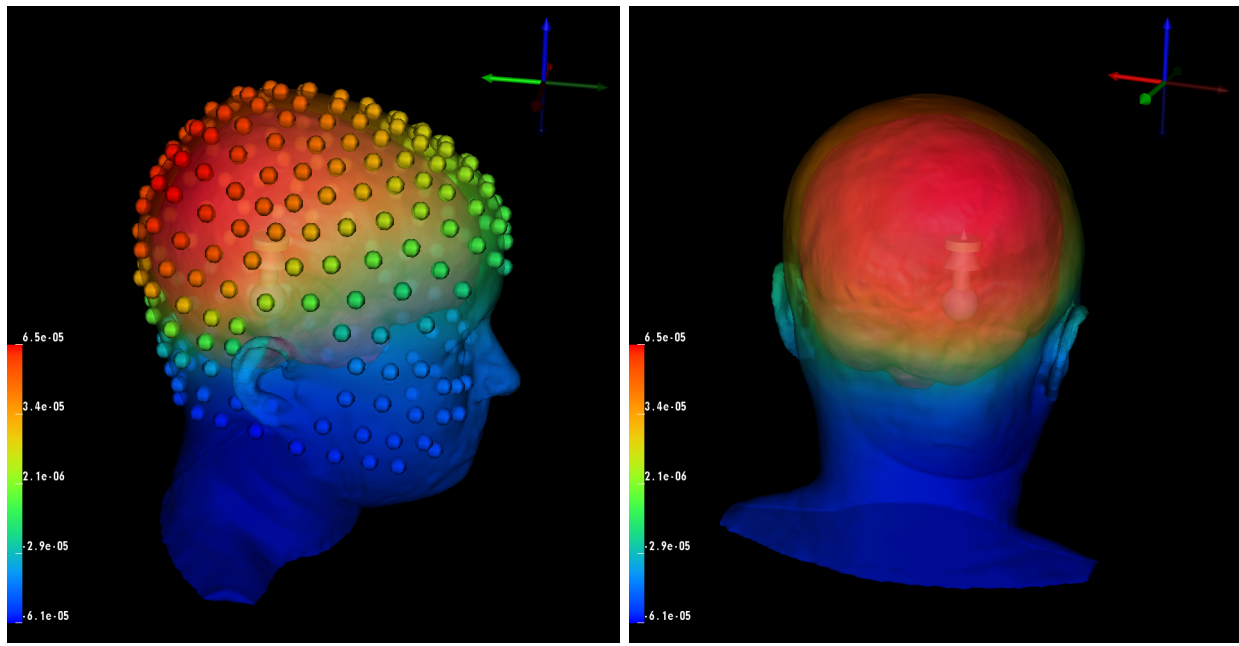


Figure 20: Isotropic forward problem solution with dipole source and data mapped onto the head surface and electrodes

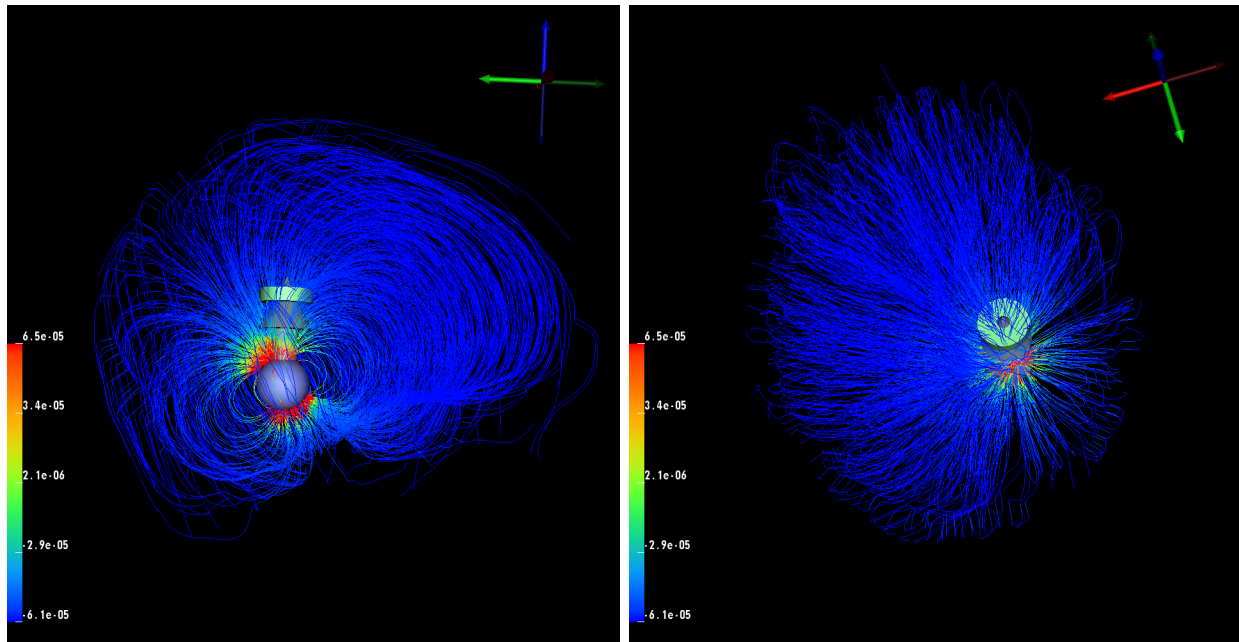


Figure 21: Isotropic streamlines with dipole source

3.3.2 Anisotropic

An anisotropic, inhomogeneous head model is expected to not have spherical propagation. This can be seen with the streamlines visualization, and even more so with isolines. As discussed in 2.5.1, there are two methods of scaling diffusion tensor data. We built the SCIRun network with the option to choose either scaling method. The simulations showed non-spherical propagation and acceptable registration of the electrodes, dipoles, and mesh into the diffusion tensor space.

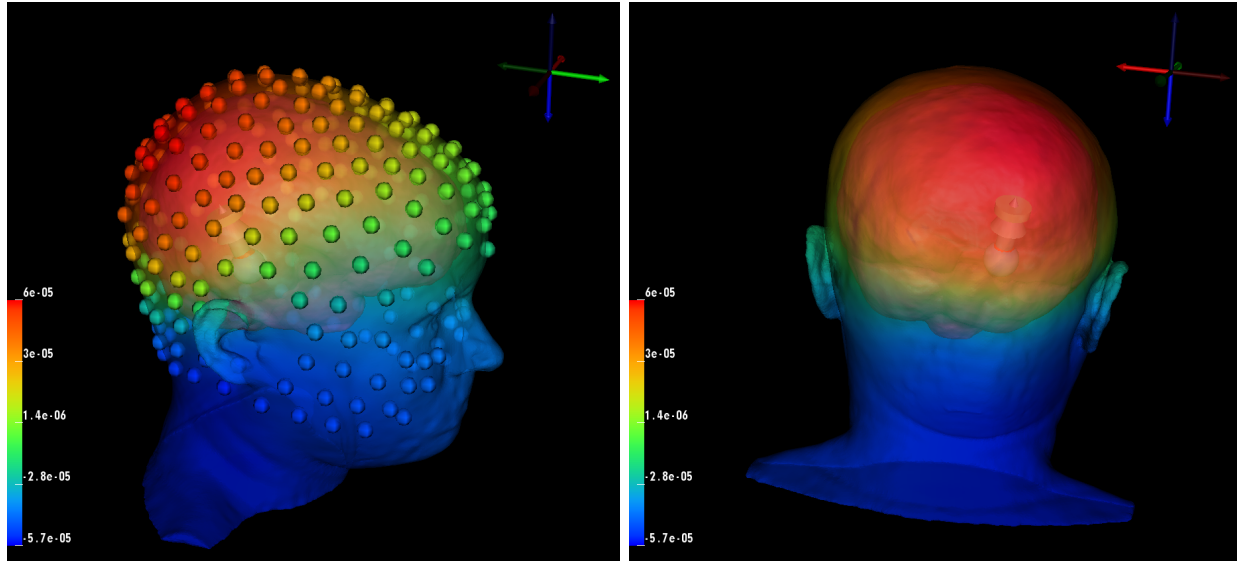


Figure 22: Anisotropic forward problem solution with dipole source and data mapped onto the head surface and electrodes

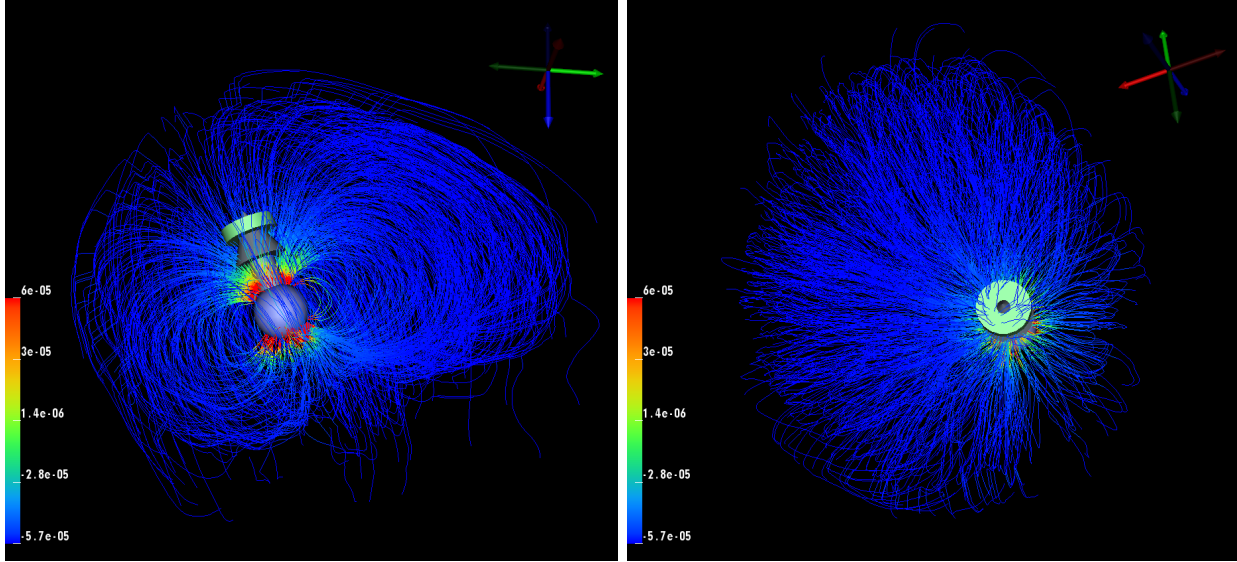


Figure 23: Anisotropic streamlines visualization with dipole source

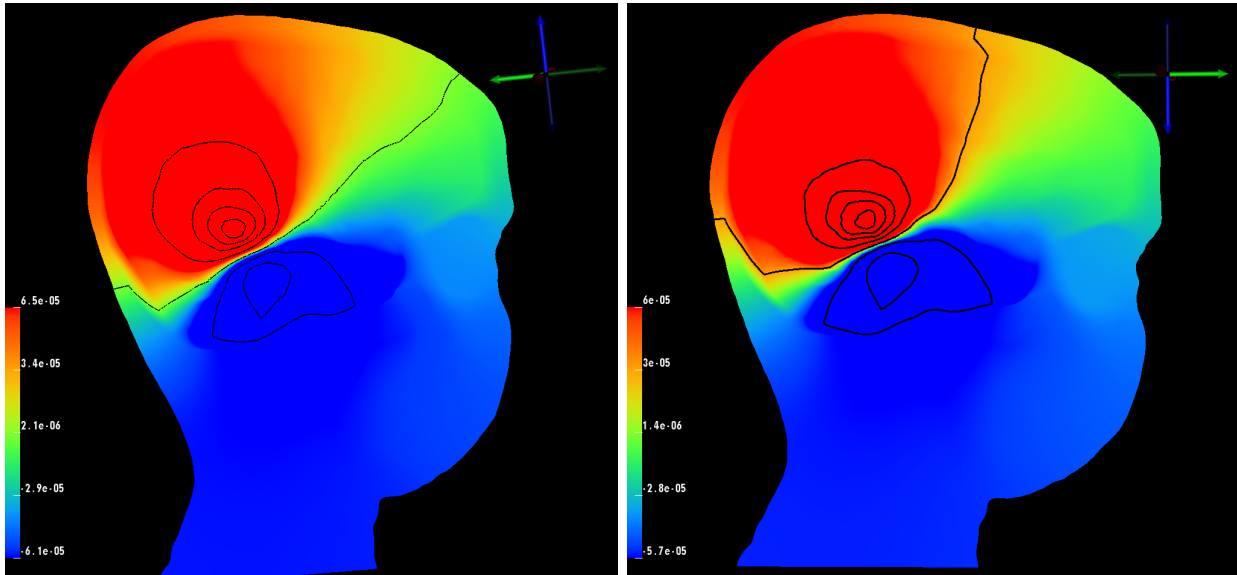


Figure 24: Isolines comparison: isotropic white matter conductivity (*left*), anisotropic white matter conductivity (*right*)

3.4 fMRI Visualization

fMRI data was a novel datatype for SCIRun. We successfully mapped and visualized the fMRI data onto the cortical surface with a rigid and manual registration to the mesh coordinate space. This allows for future use of fMRI data in simulations using the SCIRun software package.

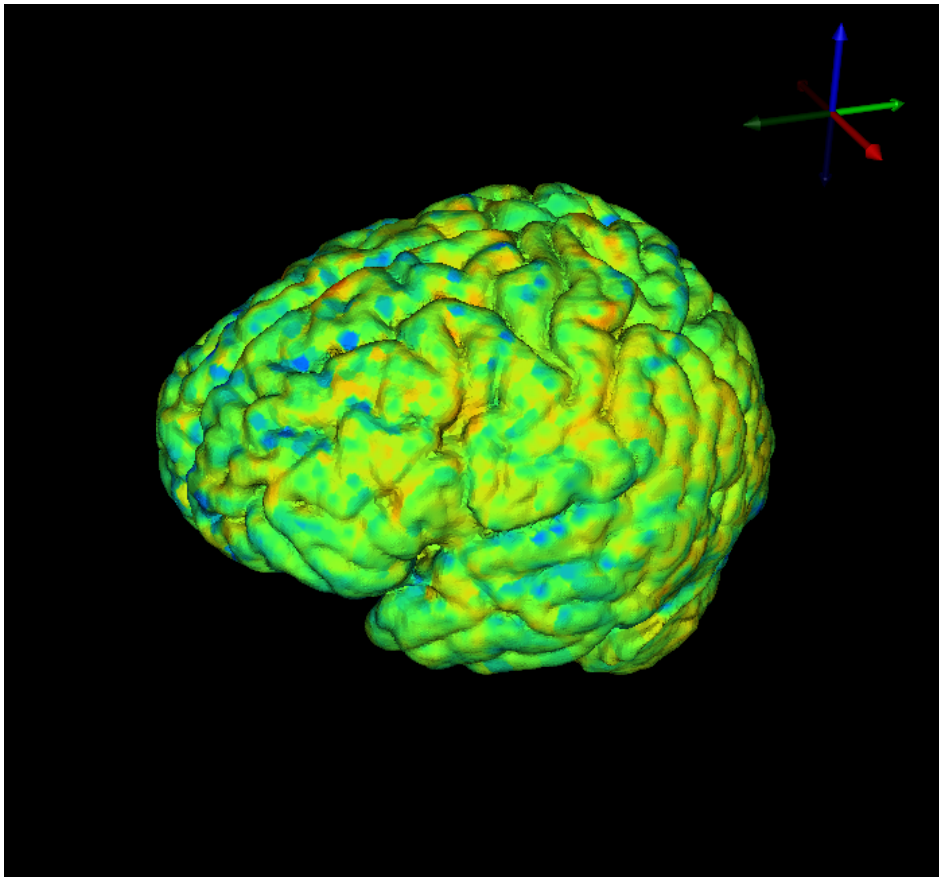


Figure 25: fMRI data mapped onto cortical surface mesh

3.5 EEG Visualization

When using EEG data, the particular application dictates if further processing, filtering, and/or cutting of the data is necessary. This dataset contained “bad” electrodes, specifically around the eyes which was possibly due to blinking or eyes rolling. The bad leads will be fixed with further specific processing or trilinear interpolation.

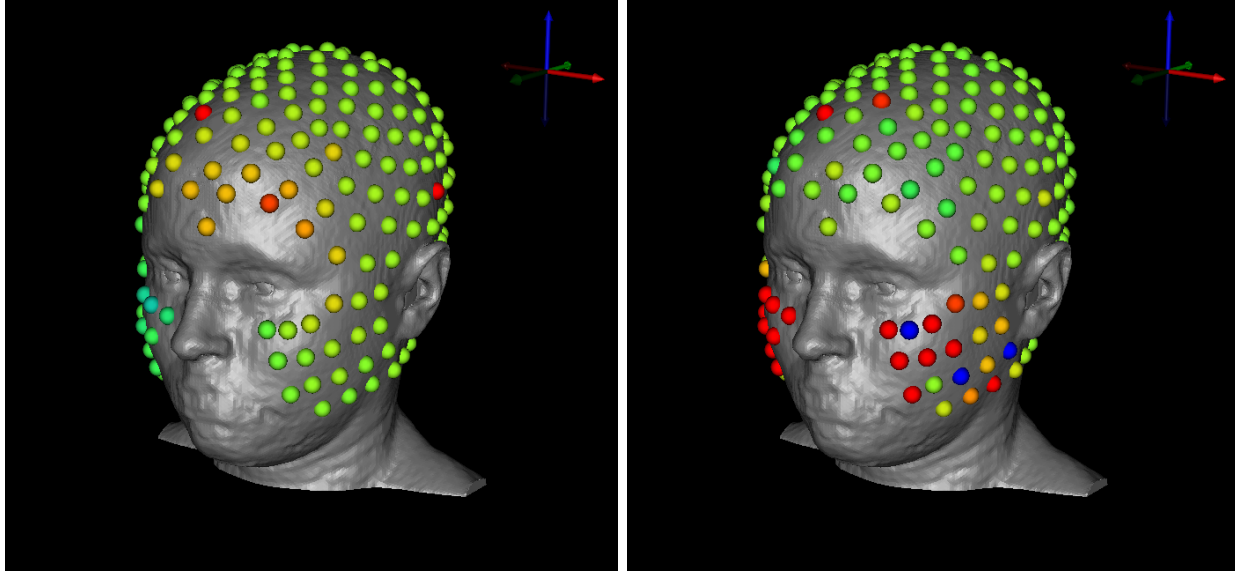


Figure 26: EEG signal visualization. Examples of “bad” electrodes that need further processing for specific applications

4 Conclusion

This paper has outlined a comprehensive pipeline to build an inhomogeneous, anisotropic head and brain model based on human data of all image modalities for use in electroencephalography with an emphasis on forward and inverse problem research as well as visualizations of function MRI data and EEG data. Along with the pipeline, the human data will be released as open-source to enable other scientists to have a starting point for further research. Building a model can be time consuming and hinder further important research. This model will allow scientists to have a straightforward path to building their own model and/or using the model because it is a product of a high-resolution, multi-image dataset.

Further investigations based on this pipeline include finding a more appropriate decimation algorithms for three-dimensional tetrahedral finite element meshes to further reduce the mesh size; more exact sinus and skull segmentation methods to improve the appearance and accuracy of these layers; and more exact registration techniques which will provide a better transformation matrix for moving images to DTI coordinate space, especially fMRI data. Additions to this dataset could include more methods to include functional MRI data into source localization simulations and more specific processing of EEG data for different applications, which will make for better visualization.

5 Acknowledgements

Imaging and electroencephalography for this project was done at Electrical Geodesics Inc. at the University of Oregon. This work could not have been completed without the help of Jess Tate and Brett Burton. This project was supported by the National Institute of General Medical Sciences

of the National Institutes of Health under grant number P41 GM103545-18.

References

- [1] R. Brette and A. Destexhe. *Handbook of Neural Activity Measurement*. Cambridge University Press, 2012.
- [2] SCI Institute, 2016. SCIRun: A Scientific Computing Problem Solving Environment, Scientific Computing and Imaging Institute (SCI), Download from: <http://www.scirun.org>.
- [3] J.P. Mugler and J.R. Brookeman. Three-dimensional magnetization-prepared rapid gradient-echo imaging (3d mp rage). *Magn. Reson. Med.*, 15(1):152–157, July 1990.
- [4] M.P. Lichy, B.M. Wietek, J.P. Mugler, W. Horger, M.I. Menzel, A. Anastasiadis, K. Siegmann, T. Niemeyer, A. Konigsrainer, B. Kiefer, F. Schink, C.D. Claussen, and H.P. Schlemmer. Magnetic resonance imaging of the body trunk using a single-slab, three-dimensional, t2-weighted turbo-spin-echo sequence with high sampling efficiency (space) for high spatial resolution imaining: initial clinical experiences. *Invest. Radiol.*, 40(12):754–760, December 2005.
- [5] T.G. Reese, O. Heid, R.M. Weisskoff, and V.J. Wedeen. Reduction of eddy-current-induced distortion in diffusion mri using a twice-refocused spin echo. *Magn. Reson. Med.*, 49(1):177–182, 2003.
- [6] J. Juntu, J. Sijbers, D.V. Dyck, and J. Gielen. Bias field correction for mri images. In: Kurzyński M., Puchała E., Woźniak M., żołnierk A. (eds) *Computer Recognition Systems. Advances in Soft Computing*, vol 30. Springer, Berlin, Heidelberg, (543-551), 2005.
- [7] Y. Zang, M. Brady, and S. Smith. Segmentation of brain mr images through a hidden markov random field model and the expectation-maximization algorithm. *IEEE Trans Med Imag*, 20(1):45–57, 2001.
- [8] J.L.R. Anderson, S. Skare, and J. Ashburner. How to correct susceptibility distortions in spin-echo echo-planar images; applications to diffusion tensor imaging. *NeuroImage*, 20(2):870–888, 2003.
- [9] S.M. Smith, M. Jenkinson, M.W. Woolrich, C.F. Beckmann, T.E.J. Behrens, H. Johansen-Berg, P.R. Bannister, M. De Luca, I. Drobnjak, D.E. Flitney, R. Niazy, J. Saunders, J. Vickers, Y. Zhang, N. De Stefano, J.M. Brady, and P.M. Matthews. Advances in functional and structural mr image analysis and implementation as fsl. *NeuroImage*, 23(S1):208–219, 2004.
- [10] X. Li, P.S. Morgan, J. Ashburner, J.C. Smith, and C. Rorden. The first step for neuroimaging data analysis: Dicom to nifti conversion. *Journal of Neuroscience Methods*, 264:47–56, 2016.
- [11] FSL. Fsl dtifit. <https://fsl.fmrib.ox.ac.uk/fsl/fslwiki/FDT/UserGuide> Section 2.4.
- [12] P.A. Yushkevich, J. Piven, H.C. Hazlett, R.G. Smith, S. Ho, J.C. Gee, and G. Gerig. User-guided 3d active contour segmentation of anatomical structures: Significantly improved efficiency and reliability. *NeuroImage*, 31(3):1116–28, July 2006.

- [13] A. Fedorov, R. Beichel, J. Kalpathy-Cramer, J. Finet, J-C. Fillion-Robin, S. Pujol, C. Bauer, D. Jennings, F.M. Fennessy, M. Sonka, J. Buatti, S.R. Aylward, J.V. Miller, S. Pieper, and R. Kikinis. 3d slicer as an image computing platform for the quantitative imaging network. *Magn. Reson. Imaging*, 30(9):1323–31, November 2012.
- [14] NITRC. 1000 functional connectomes project. http://fcon_1000.projects.nitrc.org/.
- [15] Jimmy Shen. Tools for nifti and analyze image, Jan 2014. <https://www.mathworks.com/matlabcentral/fileexchange/8797-tools-for-nifti-and-analyze-image>.
- [16] U. Aydin, J. Vorwerk, P. Kupper, M. Heers, H. Kugel, A. Galka, L. Hamid, J. Wellmer, C. Kellinghaus, S. Rampp, and C.H. Wolter. Combining eeg and meg for the reconstruction of epileptic activity using a calibrated realistic volume conductor model. *PLOS ONE*, 9(3), March 2014.
- [17] Brett Shoelson. edfread, September 2016. <https://www.mathworks.com/matlabcentral/fileexchange/31900-edfread>.
- [18] CIBC, 2016. Seg3D: Volumetric Image Segmentation and Visualization. Scientific Computing and Imaging Institute (SCI), Download from: <http://www.seg3d.org>.
- [19] S.M. Smith. Fast robust automated brain extraction. *Human Brain Mapping*, 17(3):143–155, November 2002.
- [20] A.M. Dale, B. Fischl, and M.I. Sereno. Cortical surface-based analysis. i. segmentation and surface reconstruction. *NeuroImage*, 9:179–194, 1999.
- [21] Wellcome Trust Centre for Neuroimaging. Statistical parametric mapping, May 2016. <https://www.mathworks.com/matlabcentral/fileexchange/56963-statistical-parametric-mapping>.
- [22] Koen Van Leemput, Frederik Maes, Dirk Vandermeulen, and Paul Suetens. Automated model-based tissue classification of mr images of the brain. *IEEE transactions on medical imaging*, 18(10):897–908, 1999.
- [23] A. Torrado-Carvajal, J.L. Herraiz, E. Alcain, A.S. Montemayor, L. Garcia-Cañamaque, J.A. Hernandez-Tamames, and ... & N. Malpica. Fast patch-based pseudo-ct synthesis from t1-weighted mr images for pet/mr attenuation correction in brain studies. *Journal of Nuclear Medicine*, 57(1):136–143, 2016.
- [24] CIBC, 2016. Cleaver: A MultiMaterial Tetrahedral Meshing Library and Application. Scientific Computing and Imaging Institute (SCI), Download from: <http://www.sci.utah.edu/cibc/software.html>.
- [25] C.R. Johnson. *Computational Methods and Software for Bioelectric Field Problems*, volume 1. CRC Press, 4th edition, 2015.
- [26] M. Rullmann, A. Anwander, M. Dannhauer, S.K. Warfield, F.H. Duffy, and C.H. Wolters. Eeg source analysis of epileptiform activity using a 1 mm anisotropic hexahedra finite element head model. *NeuroImage*, 44:399–410, 2009.

- [27] D. Gullmar, J. Haueisen, and J. R. Reichenbach. Influence of anisotropic electrical conductivity in white matter tissue on the eeg/meg forward and inverse solution. a high-resolution whole head simulation study. *NeuroImage*, 51:145–163, 2010.
- [28] D. Wang, R.M. Kirby, R.S. MacLeod, and C.R. Johnson. Inverse electrocardiographic source localization of ischemia: An optimization framework and finite element soltuion. *Journal of Computational Science*, 2013.
- [29] M. Jenkinson, M. Pechaud, and S. Smith. Bet2: Mr-based estimation of brain, skull and scalp surfaces. *n Eleventh Annual Meeting of the Organization for Human Brain Mapping*, 2005.

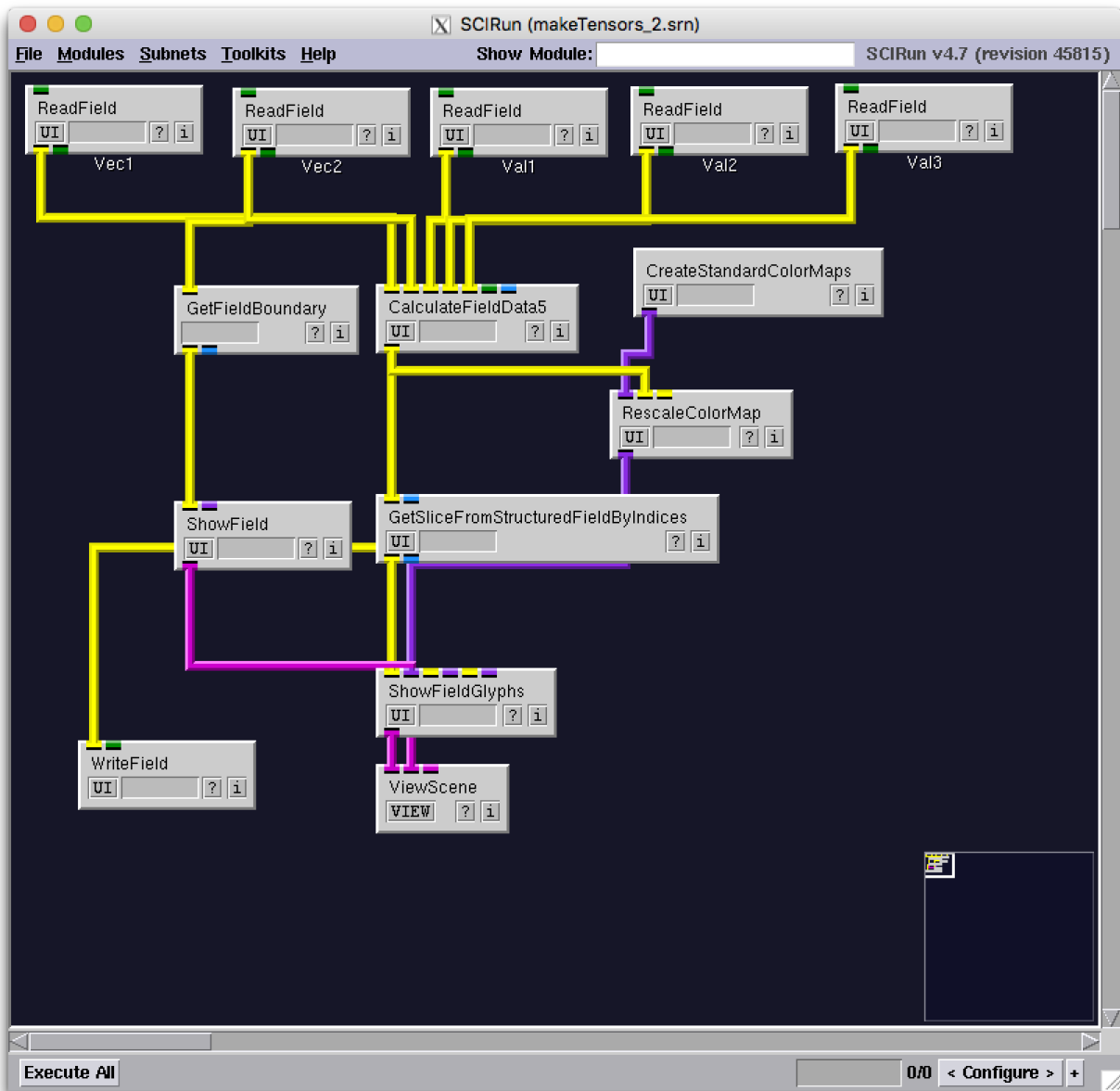


Figure 27: SCIRun network to build diffusion tensor dataset

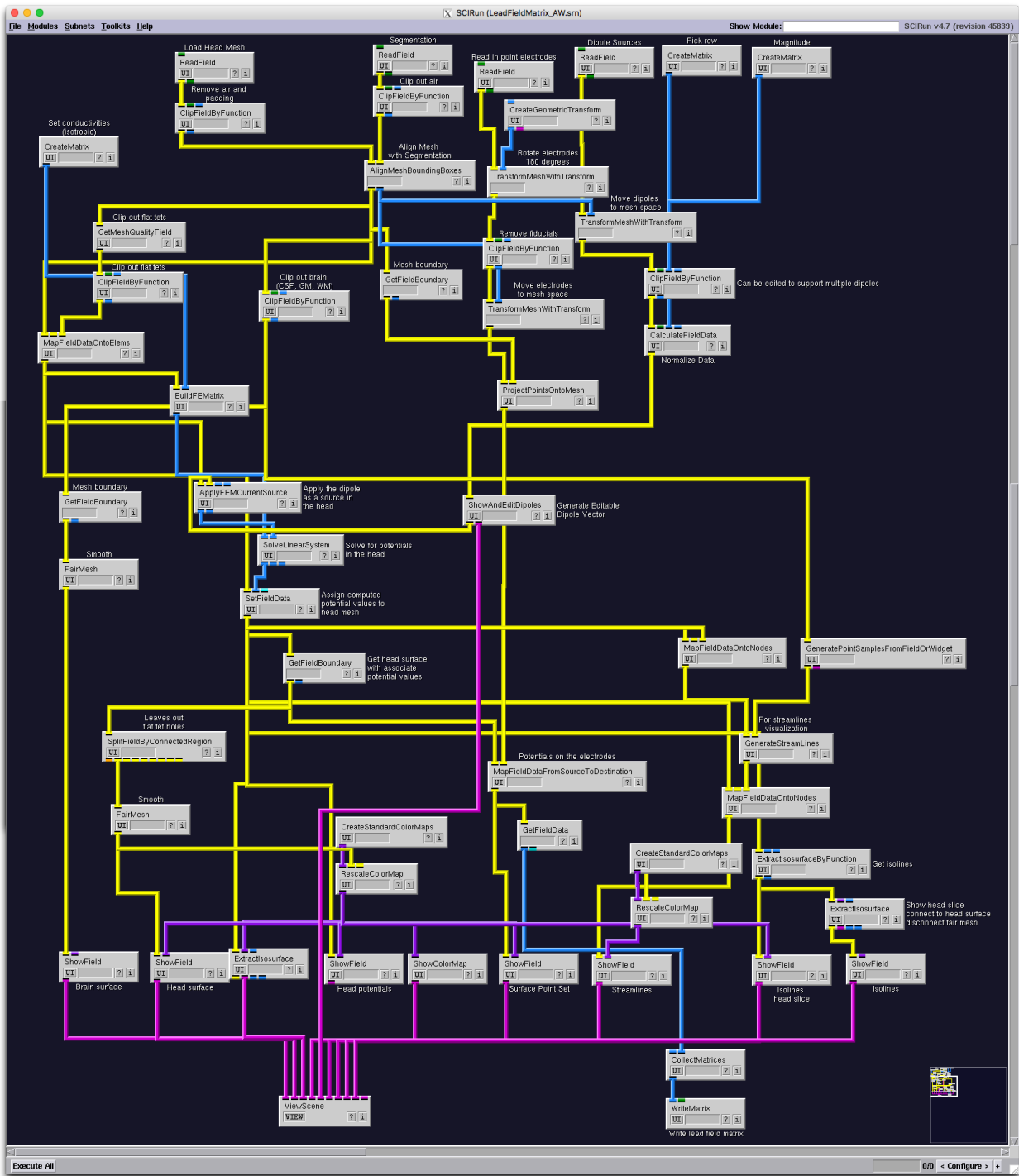


Figure 28: SCIRun Network for Isotropic Forward Problem

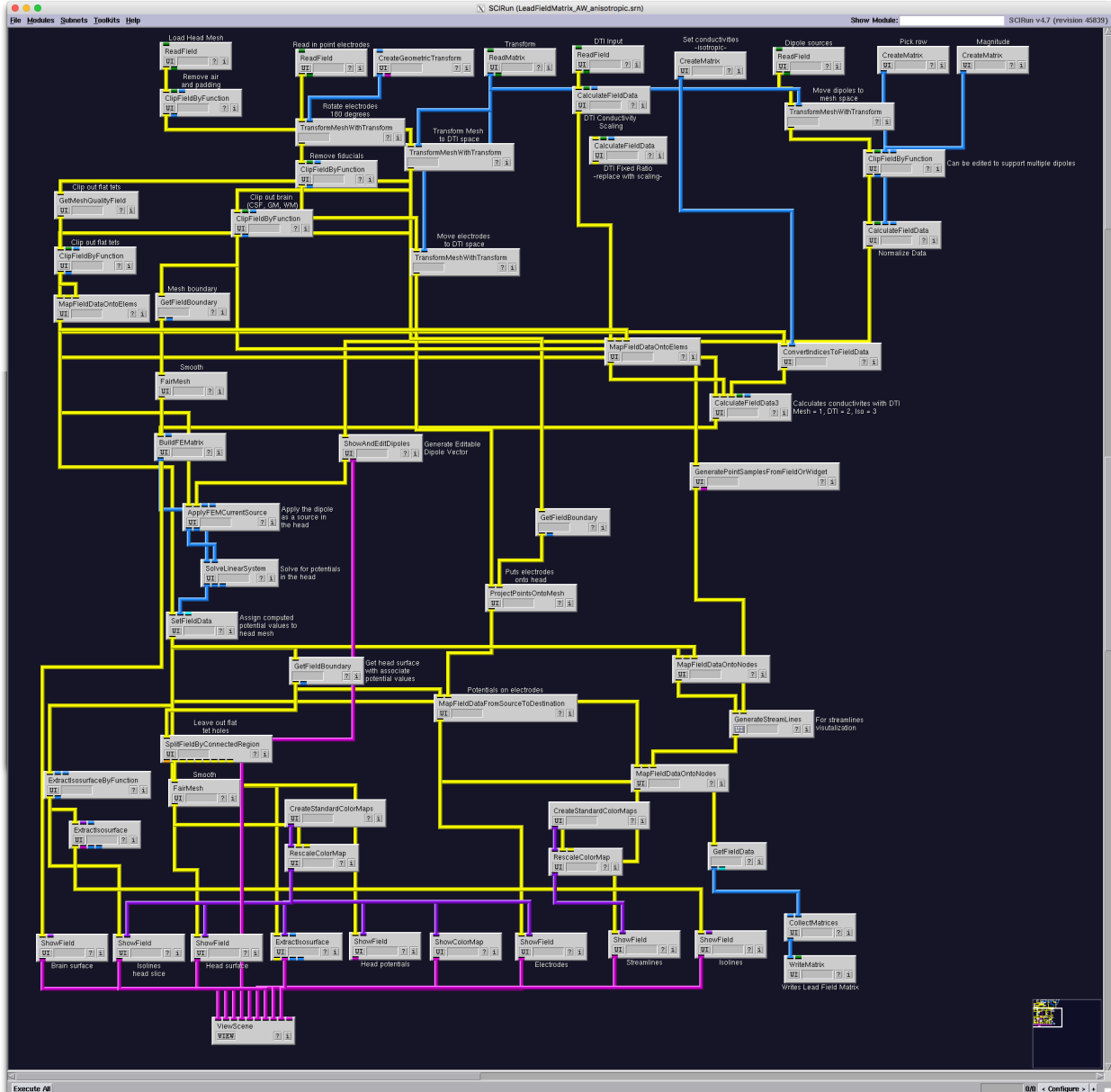


Figure 29: SCIRun Network for Anisotropic Forward Problem

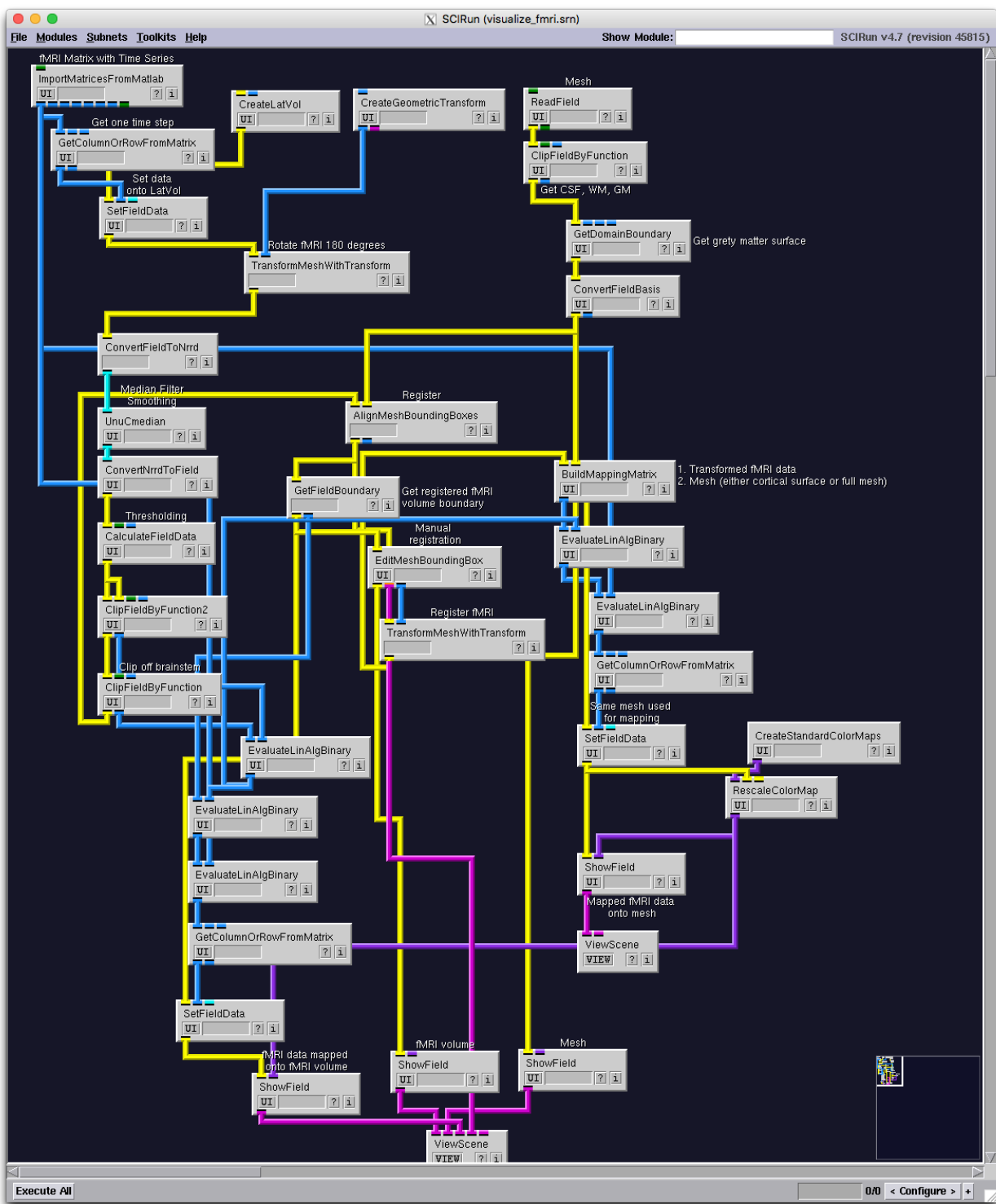


Figure 30: SCIRun Network for fMRI Visualization

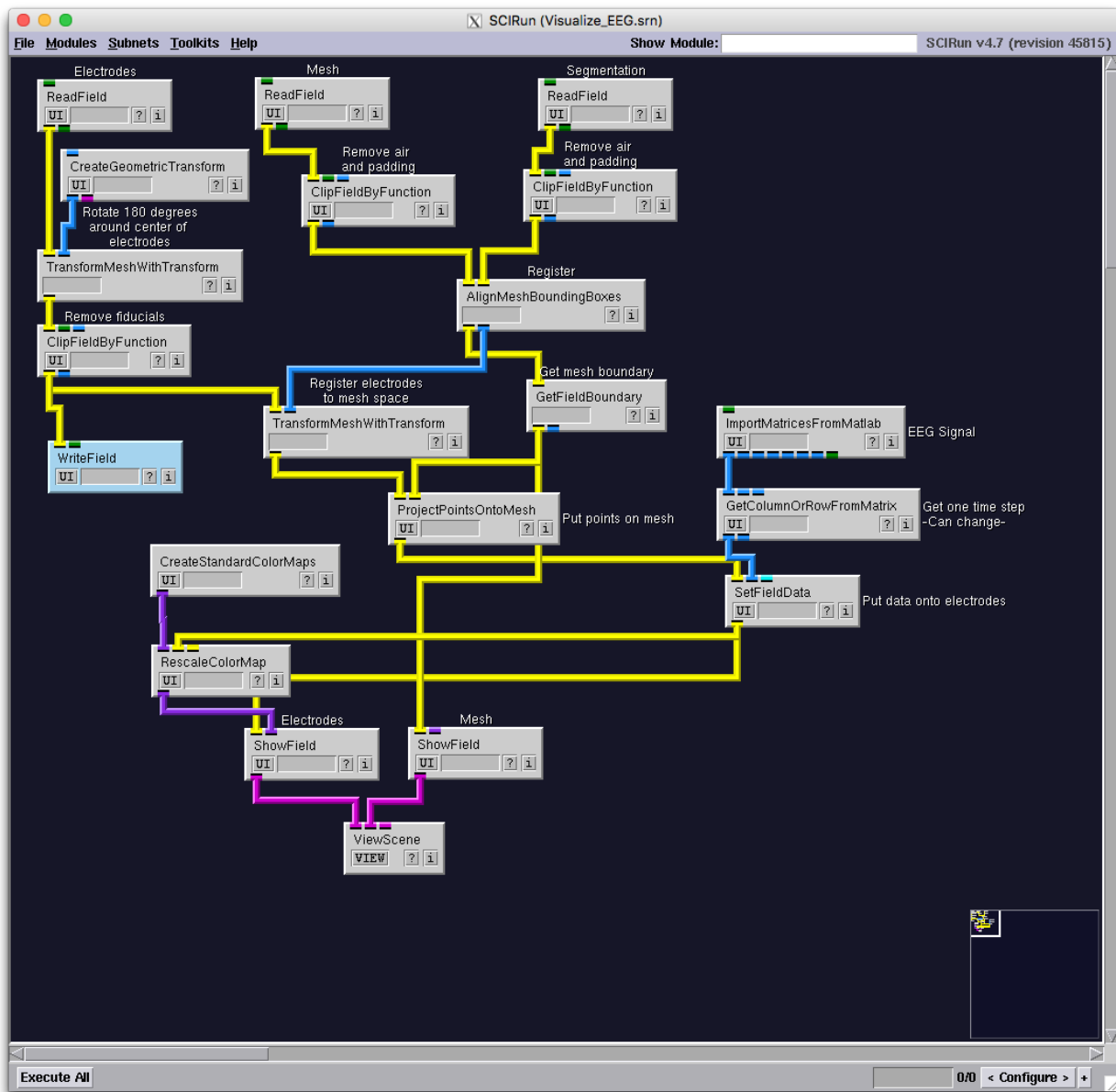


Figure 31: SCIRun Network for EEG Visualization